



Comparative Study on Corrosion Behavior and Mechanism of As-Cast Mg–Zn–Y and Mg–Zn–Gd Alloys

Guoqiang Xi¹ · Xuhan Zhao¹ · Yanlong Ma¹ · Yu Mou¹ · Ju Xiong¹ · Kai Ma² · Jingfeng Wang²

Received: 31 May 2022 / Revised: 10 July 2022 / Accepted: 11 July 2022 / Published online: 10 September 2022
© The Chinese Society for Metals (CSM) and Springer-Verlag GmbH Germany, part of Springer Nature 2022

Abstract

Rare earth (RE) elements have large solid solubility in magnesium and are widely used to regulate the microstructure and property of advanced magnesium alloys. However, different kinds of RE elements have different effects on microstructure and property of the alloy. In this study, a Mg–Zn–Y alloy and a Mg–Zn–Gd alloy with alloying elements of the same atomic percentage were designed to clarify the effect of yttrium (Y) and gadolinium (Gd) on the corrosion behavior of as-cast MgZn₂Y_{2.66} and MgZn₂Gd_{2.66} alloys. The results show that the MgZn₂Y_{2.66} alloy is mainly composed of α -Mg phase and long period stacking ordered (LPSO) phase, while MgZn₂Gd_{2.66} alloy is mainly composed of α -Mg phase and (Mg, Gd)₃Zn phase (W phase). Generally speaking, the corrosion phenomena of the two alloys in 3.5 wt% NaCl solution are similar. In the early stages of exposure, the alloys underwent uniform corrosion at a relatively low corrosion rate. With prolonged exposure, localized corrosion became dominated and the corrosion rate was greatly increased. However, the corrosion rate of the MgZn₂Y_{2.66} alloy, in terms of the corrosion current density, is about one order of magnitude lower than that of the MgZn₂Gd_{2.66} alloy. The high corrosion resistance of the MgZn₂Y_{2.66} alloy is mainly attributed to the presence of LPSO phase in form of continuous networks and the relatively high corrosion resistance of the corrosion product layer on the alloy.

Keywords Magnesium alloys · Rare earth · Long period stacking ordered (LPSO) phase · Microstructure · Corrosion

1 Introduction

As the lightest structural material, magnesium alloys not only have high specific strength and specific stiffness but also have good castability, machinability, thermal conductivity, electromagnetic shielding ability and excellent damping characteristic, which makes magnesium alloys promising candidate materials in the fields of aerospace, automobile and electronics [1–4]. However, the application of magnesium alloys is limited due to their relatively low absolute strength, insufficient ductility, and poor corrosion resistance. It is reported that adding an appropriate amount of rare earth (RE) elements into magnesium alloys is an effective

way to improve the comprehensive properties of magnesium alloys [5, 6]. Of all RE-containing magnesium alloys, Mg–RE–Zn systems have attracted extensive attention due to their excellent mechanical properties and creep resistance [7–9]. Mg–RE–Zn alloys can be divided into two types according to whether there is long period stacking ordered (LPSO) phase in as-cast state [10–13]. For TypeIMg–RE–Zn alloys, LPSO phase forms at grain boundaries during the casting process (RE = Y, Dy, Ho, Er, and Tm). For TypeIIMg–RE–Zn alloys, LPSO does not form during the casting process but forms in the subsequent annealing process (RE = Gd and Tb).

Gadolinium (Gd) has very high solubility in magnesium alloys (23.5 wt% at the eutectic temperature) and, therefore, the Mg–Zn–Gd alloy system is an important alloy system among RE-containing magnesium alloys. Liu et al. [14] found that, with the increase of Gd content in Mg–Gd–Zn alloys, the alloy microstructure was gradually refined and the compression performance at room temperature was gradually enhanced. Wang et al. [15] found that addition of Gd to magnesium alloys would inhibit dynamic recrystallization and increase texture intensity, leading to improved

Available online at <http://link.springer.com/journal/40195>.

✉ Yanlong Ma
myl@cqut.edu.cn

¹ College of Material Science and Engineering, Chongqing University of Technology, Chongqing 400054, China

² College of Materials Science and Engineering, Chongqing University, Chongqing 400044, China

mechanical properties; the Mg–Gd–Zn alloy with 2 wt% Gd exhibited a yield strength of 369.8 MPa and ultimate tensile strength of 400.3 MPa. Similarly, Sabbagian et al. [16] found that, by adding 1 wt% Gd to the Mg–Zn alloy system, the average grain size was reduced from 14.6 to 5.7 μm ; the yield strength was increased from 198 to 241 MPa; and the ultimate tensile strength was increased from 301 to 336 MPa.

Compared with the Mg–Zn–Gd alloy system, the Mg–Zn–Y alloy system has attracted more attention due to the presence of LPSO phase in the as-cast state [17]. It is reported that the Mg–Zn–Y alloy prepared by rapid powder metallurgy process shows a yield strength of 600 MPa and an elongation of 5% at room temperature due to the presence of fine LPSO phase at grain boundaries [18, 19]. The LPSO phase could enhance the alloy strength through short-fiber strengthening mechanism [20, 21]. Further, the LPSO phase would accommodate the stress concentration and coordinate plastic deformation of the alloy, leading to improved plasticity before cracking.

In addition to mechanical properties, corrosion resistance of RE-containing magnesium alloys is another important issue [22, 23]. It is generally believed that the micro-galvanic corrosion between the second phase and the magnesium matrix is a key factor affecting the corrosion resistance of the magnesium alloy [24–28]. Some studies show that the addition of Gd and Y can improve the microstructure of magnesium alloys and weaken the micro-galvanic corrosion. For instance, Zhang et al. [29] found that LPSO phase in the Mg–Zn–Y alloy was more difficult to corroded than the matrix, so it could work as a barrier between the matrix and eutectic phase. Zhang et al. [30] elucidated that minor Gd addition in MgZn_1Y_2 (at.%) could refine the grain size and form complete network eutectic and large volume fraction of LPSO phase, resulting in enhanced corrosion resistance. However, the detrimental effect of RE-containing phases on corrosion resistance of magnesium alloys has also been frequently reported. Srinivasan et al. [31] studied the corrosion behavior of Mg–Gd–Zn alloy in NaCl solution and found that the relatively discrete network structure became continuous with the increase of Gd content. At the same time, with the increase of the volume of the second phases ($(\text{Mg}, \text{Zn})_3\text{Gd}$ and LPSO), serious micro-galvanic corrosion occurred and the corrosion rate increased. Liu et al. [32] observed that the accelerated corrosion rate of the cast Mg–2Zn–15Gd–0.39 Zr alloy was mainly attributed to the presence of micro-cathodes, such as $(\text{Mg}, \text{Zn})_3\text{Gd}$ eutectic phase and the LPSO phase.

The literature review suggests that the effect of Gd and Y on the corrosion behavior of RE-containing magnesium alloys varies with alloying element content, the type and distribution of the second phase. This is probably why there are many arguments regarding the effect of Gd and Y on

the corrosion behavior of RE-containing magnesium alloys. Therefore, in present study, the corrosion behavior of the Mg–Zn–Y and Mg–Zn–Gd alloys with the same element content (at.%) was studied comparatively. We found that the corrosion rate of the $\text{MgZn}_2\text{Y}_{2.66}$ alloy, in terms of the corrosion current density, was about one order of magnitude lower than that of the $\text{MgZn}_2\text{Gd}_{2.66}$ alloy. The high corrosion resistance of the $\text{MgZn}_2\text{Y}_{2.66}$ alloy was mainly attributed to the presence of LPSO phase in form of continuous networks and the relatively high corrosion resistance of the corrosion product layer on the alloy.

2 Experimental

2.1 Material Preparations

The $\text{MgZn}_2\text{Y}_{2.66}$ and $\text{MgZn}_2\text{Gd}_{2.66}$ alloys were obtained by melting pure Mg (99.9 wt%), Mg–26.38 wt% Gd, Mg–21.5 wt% Y and pure Zn in a resistance furnace with CO_2 and SF_6 protection gas. Firstly, the surface of the master alloys was fully polished to remove the oxide film. Then the polished alloy, pure Mg and pure Zn were put into a stainless steel crucible and then heated in a resistance furnace. The cast alloy was obtained by keeping the melt at 750 $^\circ\text{C}$ for 25 min and then cooled in a saltwater bath. Table 1 lists the actual chemical composition of these alloys. Samples for microstructural characterization, electrochemical measurements and immersion tests were prepared from the ingots. Each sample was sequentially grinded with sandpapers from 320# to 3000#, ultrasonically cleaned in distilled water, and then dried in a cool air stream.

2.2 Microstructural Characterization

Samples for microstructural observation were first mechanically ground using SiC sandpapers and then electrochemically polished in commercial AC2 solution for 2 min at 20 V. The microstructure of the alloys was examined in a Zeiss Sigma HD field emission gun scanning electron microscope (FEG-SEM) equipped with Oxford energy dispersive spectroscopy (EDS). The alloy phases in the alloys were analyzed using PANalytical-Empyrean X-ray diffraction (XRD), with a copper target, with a scanning angle range of 20 $^\circ$ –90 $^\circ$ and a scanning speed of 2 $^\circ$ /min.

Table 1 Chemical composition of the alloys

Alloy	Mg (wt%)	Gd (wt%)	Y (wt%)	Zn (wt%)
$\text{MgZn}_2\text{Y}_{2.66}$	Bal	–	7.43	4.20
$\text{MgZn}_2\text{Gd}_{2.66}$	Bal	12.40	–	3.28

2.3 Immersion Test

The immersion test was carried out in 3.5 wt% NaCl solution at room temperature. During the immersion process, a stereo microscope (SMZ, SZN71) was used to observe and record the macroscopic corrosion morphology of the sample surfaces. Further, the hydrogen evolution test and mass loss test were performed on parallel samples immersed in 3.5 wt% NaCl solution at room temperature for 24 h. After immersion, the corrosion products were collected. Their chemical composition and chemical state were analyzed by an X-ray photoelectron spectroscope (XPS, Thermofisher, ESCALAB, 250Xi) with an Al $K\alpha$ X-ray radiation source. The surface and cross-sectional morphology of selected samples were examined by FEG-SEM. The cross sections of the samples were prepared by ultramicrotomy (Leica Ultracut). The corrosion products of selected samples were removed by immersing the samples in a mixed solution containing 200 g/L chromic acid and 10 g/L of AgNO_3 according to the national standard GB/T16545-1996.

2.4 Electrochemical Measurements

Electrochemical measurements were carried out on a Gamry Reference 3000 potentiostat at room temperature in 3.5 wt% NaCl solution. The sample, a platinum plate and a saturated calomel electrode were used as the working electrode, counter electrode and reference electrode, respectively. Potentiodynamic polarization and electrochemical impedance spectroscopy tests were conducted after immersion in the solution for 300 s to obtain a relatively stable surface condition.

3 Results

3.1 Microstructure Observation

Figure 1 shows backscattered electron micrographs of the as-cast alloys, where the alloy matrix was revealed as dark areas while the second phases were revealed as bright areas. The morphology and distribution of second phases were distinctly different in the two alloys. The major second phase in the Mg–Zn–Y alloy had a lamellar structure and was

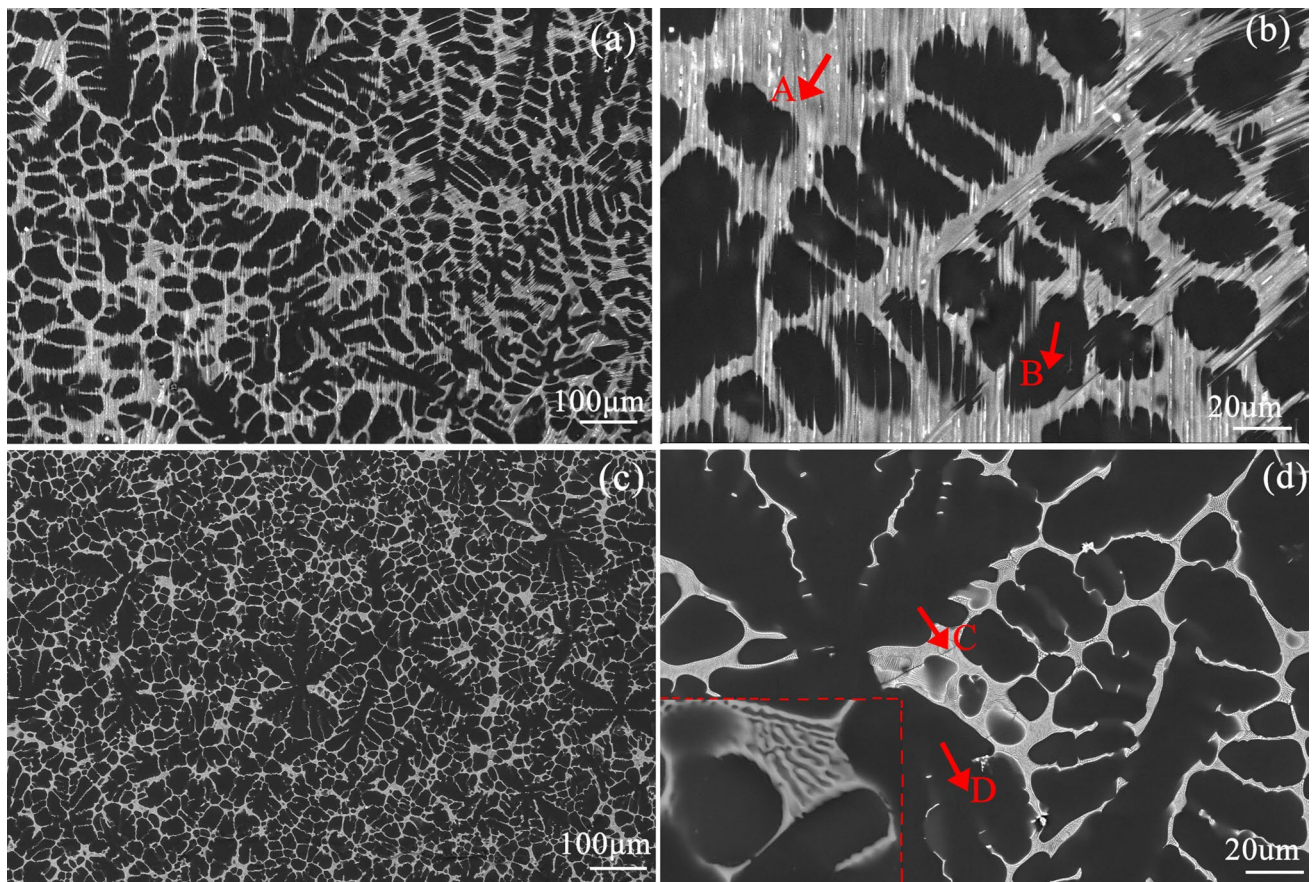


Fig. 1 Backscattered SEM images of as-cast $\text{MgZn}_2\text{Y}_{2.66}$ alloy **a, b** and $\text{MgZn}_2\text{Gd}_{2.66}$ alloy **c, d**

distributed in a network along the grain boundary (Fig. 1a, b). In contrast, the major second phase in the Mg–Zn–Gd alloy was in fishbone-like form (Fig. 1c, d) and was distributed discontinuously along grain boundaries. Table 2 lists the EDS analysis results of points A, B, C and D in Fig. 1, corresponding to the major second phase and solid solution in the two alloys, respectively. Combining with the EDS analysis, the XRD analysis (Fig. 2) and literature reports, it can be inferred that the lamellar phase in Mg–Zn–Y alloy is Mg_{12}YZn (LPSO) phase [33] and the fishbone-like phase in Mg–Zn–Gd alloy is $(\text{Mg}, \text{Zn})_3\text{Gd}$ (W phase) [34, 35].

3.2 Corrosion Behavior

3.2.1 Immersion and Hydrogen Test

Figure 3 shows surface morphology of the alloy recorded in situ when the alloys were immersed in 3.5 wt% NaCl solution. At the initial stage of immersion (~3 min), many bubbles appear on the surface of both alloys, and there are fewer bubbles on Mg–Zn–Y alloy (Fig. 3a) than Mg–Zn–Gd alloy (Fig. 3b). With the increase of immersion time, the number of bubbles on the alloy surface decreases and the size increases gradually (~15 min). After that, the number

of bubbles on the alloy surface further reduced and eventually disappeared. At the same time, localized corrosion characterized by stable gas streams appeared on the alloy surfaces. It can be known from the principle of corrosion electrochemistry that the bubbles and gas streams formed during the immersion process are related to hydrogen gas formed at the cathode when the magnesium alloy dissolves at the anode.

The uniformly-distributed gas bubbles on the alloy surface in the early state of immersion suggest uniform corrosion at the moments, and the corrosion rate is low. Thereafter, with the formation and thickening of the corrosion product layer, the uniform corrosion rate of the alloy decreased. Consequently, the number of the gas bubbles on the surface also decreased, and some small bubbles merged and grew into larger bubbles. When the immersion process was further extended, the corrosion form changed from uniform corrosion to localized corrosion. At this time, the corrosion concentrated in local parts of the alloy, which resulted in anodic dissolution of these parts and cathodic protection of the surrounding regions.

Figure 4a, b shows the volume of hydrogen gas vs. immersion time of the alloys recorded during immersion in the NaCl solution for up to 24 h. The volume of the hydrogen gas was small for both alloys in the first 2 h of immersion, suggesting relatively low corrosion rate. After that, the volume of the hydrogen gas increased with immersion time for both alloys. However, the increasing rates are different. For the $\text{MgZn}_2\text{Y}_{2.66}$, the volume of the hydrogen gas increased at a relatively low rate during the whole course of the immersion. In contrast, the volume of the hydrogen gas for the $\text{MgZn}_2\text{Gd}_{2.66}$ increased quickly between 2 and 8 h of immersion, suggesting fast

Table 2 EDS elemental analysis of the phase marked in Fig. 1

Position	Element (at.%)			
	Mg	Gd	Y	Zn
A	87.2	–	7.9	4.8
B	98.5	–	0.9	0.4
C	90.4	5.0	–	4.4
D	99.1	0.3	–	0.5

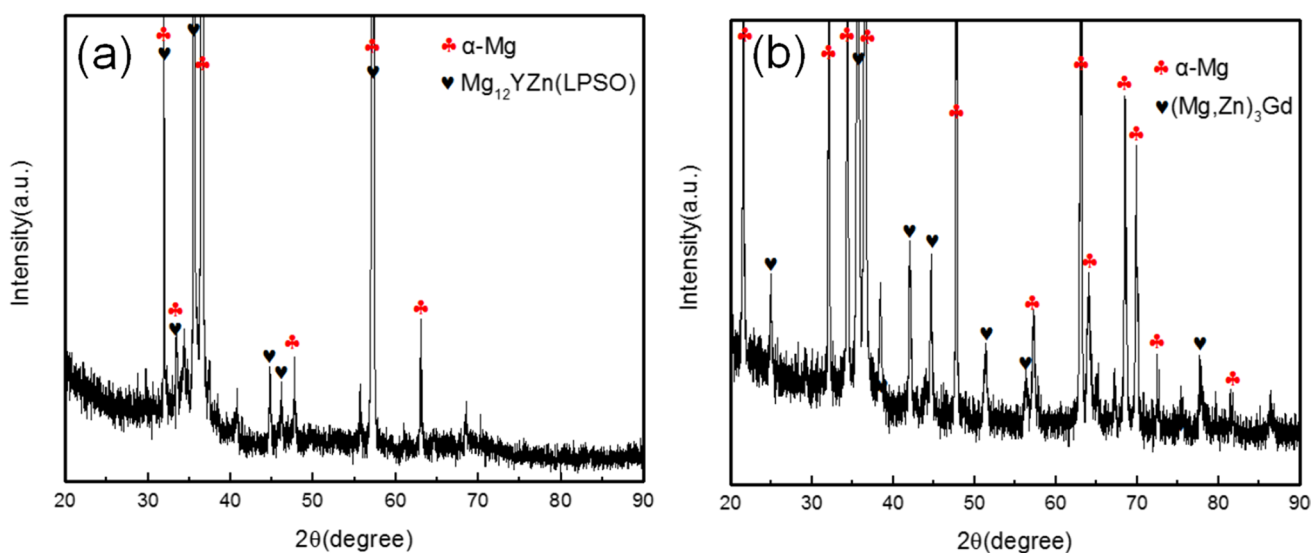


Fig. 2 XRD patterns of alloy: **a** $\text{MgZn}_2\text{Y}_{2.66}$, **b** $\text{MgZn}_2\text{Gd}_{2.66}$

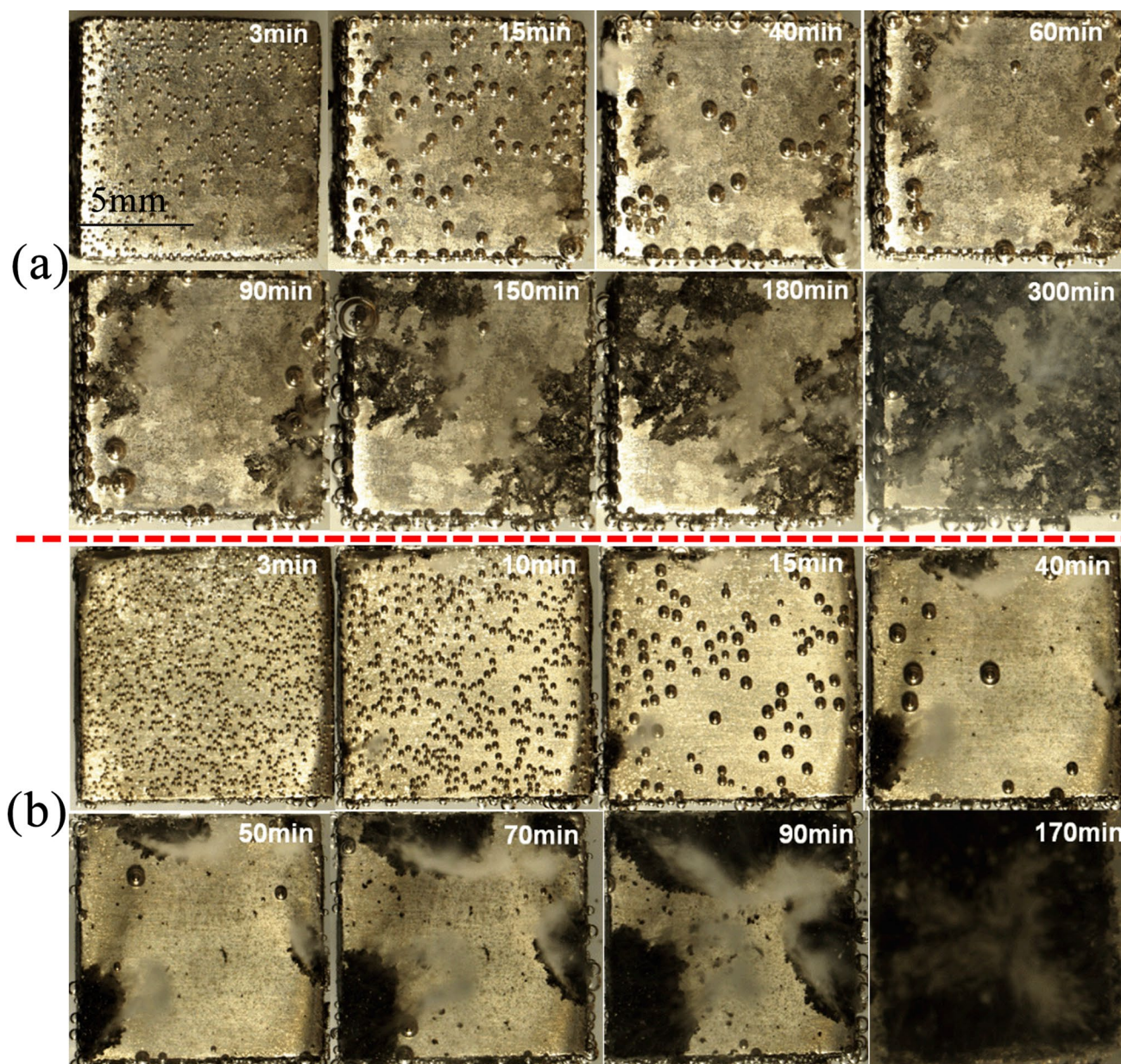


Fig. 3 Macroscopic corrosion morphologies of the two alloys in 3.5 wt% NaCl solution: **a** MgZn₂Y_{2.66} alloy, **b** MgZn₂Gd_{2.66} alloy

propagation of corrosion attack in the alloy. Beyond that, the volume of the hydrogen gas increased at a slightly-reduced rate, suggesting slightly reduced corrosion rate. As discussed later, this is probably related to the formation of the corrosion product layer. Figure 4c shows the mass loss of the alloys after immersion in the NaCl solution for 24 h. The total mass loss of the MgZn₂Gd_{2.66} alloy is about 6 times that of the MgZn₂Y_{2.66} alloy, suggesting much higher corrosion rate of the MgZn₂Gd_{2.66} alloy compared with the MgZn₂Y_{2.66} alloy.

3.2.2 Electrochemical Test

In order to assist the understanding of the corrosion mechanism of the alloys, electrochemical measurements were carried out. Figure 5a shows the open circuit potentials (OCPs) of the two alloys recorded during immersion in the NaCl solution for up to 300 min. The OCP of the Mg–Zn–Y alloy increased rapidly from -1.72 to -1.54 V and then decreased to -1.60 V in the initial stages of immersion (0–20 min). Thereafter, the OCP fluctuated around -1.60 V with the extension of the immersion time. In contrast, the

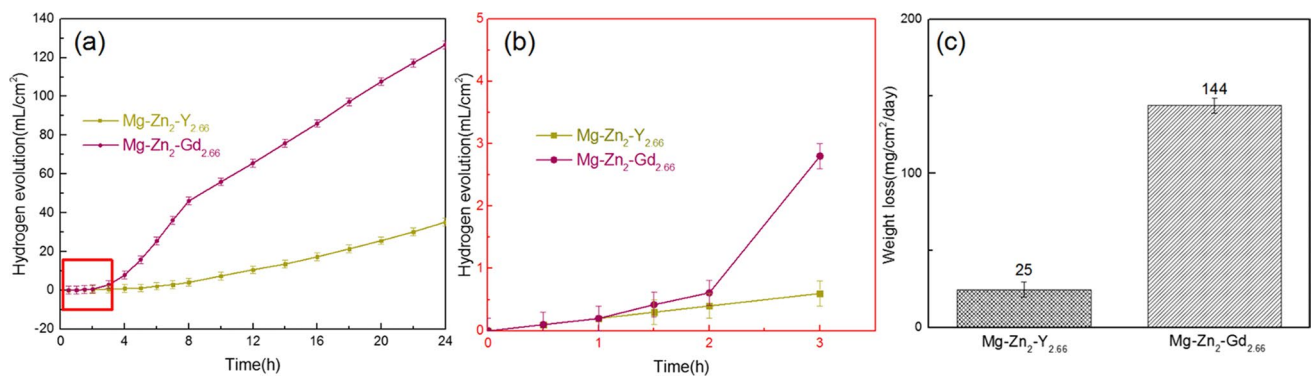


Fig. 4 **a** Average hydrogen evolution of studied alloys in 3.5 wt% NaCl solution, **b** the enlargement of the red rectangle region in **a**; and **c** mass loss rate of studied alloys in 3.5 wt% NaCl solution

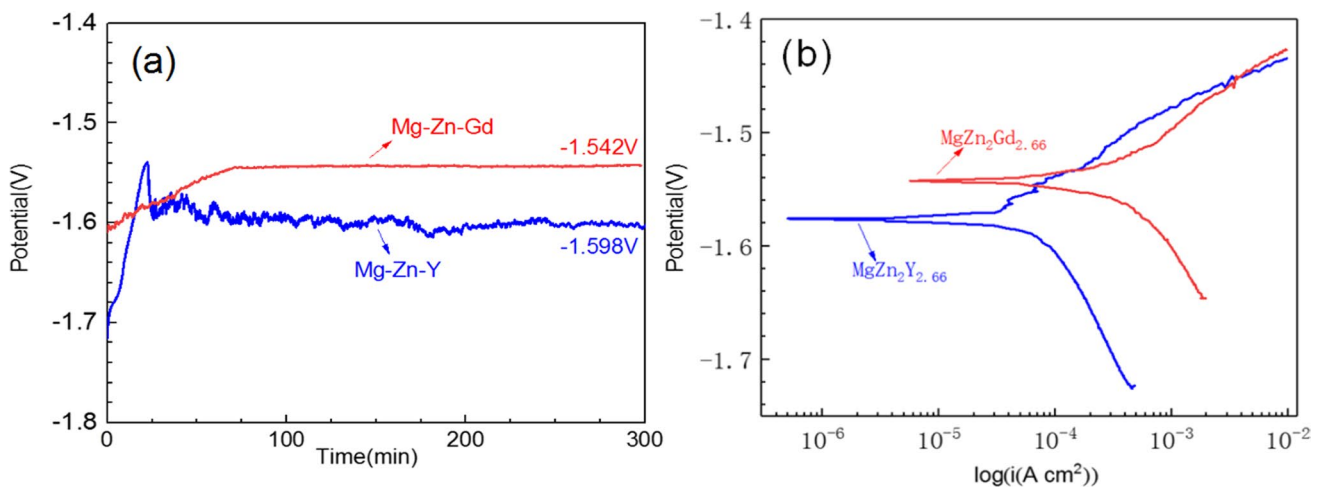


Fig. 5 **a** Open circuit potential and **b** potentiodynamic polarization curves of the two alloys in 3.5 wt% NaCl solution

OCP of the Mg–Zn–Gd alloy increased at reduced rates from -1.61 to -1.54 V within 60 min and then stabilized. The increase of OCP at the initial stage indicates that a corrosion product layer has been formed on the alloy surfaces. The increasing rate of the OCP reflects the increasing resistance of the corrosion product layer which is determined by the composition, compactness, and thickness of the corrosion product layer. The relatively higher stabilized OCP of the Mg–Zn–Gd alloy relative to the Mg–Zn–Y alloy is probably associated with the relatively more positive standard electrode potential of Gd/Gd^{+3} (-2.28 V) compared with that of Y/Y^{+3} (-2.37 V) [36].

Figure 5b shows potentiodynamic polarization curves of the two alloys in the NaCl solution. Compared with Mg–Zn–Gd alloy, the polarization curve of Mg–Zn–Y alloy was significantly shifted to the left, suggesting higher corrosion resistance of the Mg–Zn–Y alloy relative to the Mg–Zn–Gd alloy. The corrosion potentials and corrosion current densities of the two alloys obtained by Tafel fitting of

Table 3 Corrosion potentials and corrosion current densities of the two alloys obtained by Tafel fitting of the potentiodynamic polarization curves

Alloy	Corrosion current density (A/cm^2)	Corrosion potential (V)
$\text{MgZn}_2\text{Y}_{2.66}$	1.02×10^{-5}	-1.579
$\text{MgZn}_2\text{Gd}_{2.66}$	3.24×10^{-4}	-1.551

the data are listed in Table 3. The corrosion current density of the Mg–Zn–Y alloy was one order of magnitude lower than that of the Mg–Zn–Gd alloy.

The electrochemical impedance spectra of the two alloys after immersion in 3.5 wt% NaCl solution for 5 min are shown in Fig. 6. The Nyquist plots of the $\text{MgZn}_2\text{Y}_{2.66}$ alloy displayed one capacitive loop at high and intermediate frequencies, while the Nyquist plots of $\text{MgZn}_2\text{Gd}_{2.66}$ alloy displayed one capacitive loop at high and intermediate

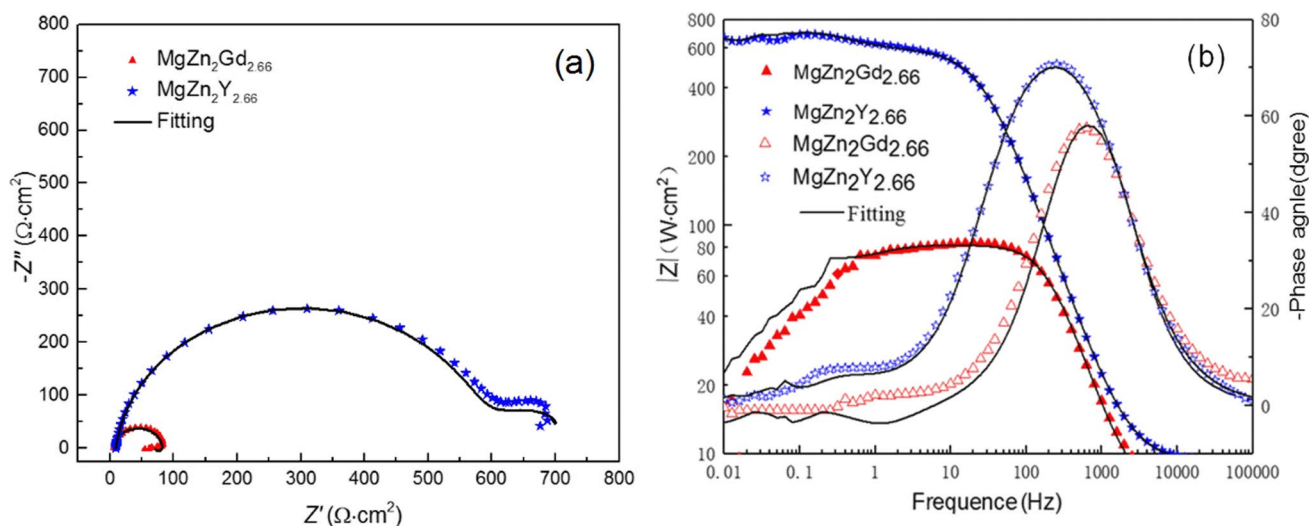


Fig. 6 Electrochemical impedance spectra (EIS) of the two alloys after immersion in 3.5 wt% NaCl solution for 5 min: **a** Nyquist diagram, **b** Bode diagram

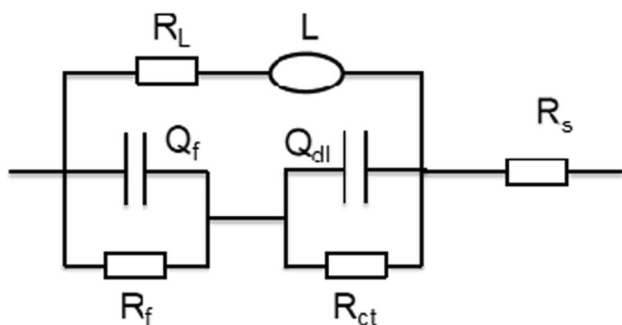


Fig. 7 Equivalent circuit used to fit the EIS shown in Fig. 6

frequencies and an inductive loop at low frequencies. In the Bode plots, the $\text{MgZn}_2\text{Y}_{2.66}$ alloy shows relatively high impedance at low frequencies, suggesting formation of a continuous corrosion product layer; while the impedance of the $\text{MgZn}_2\text{Gd}_{2.66}$ alloy dropped dramatically at low frequencies, suggesting initiation and propagation of localized corrosion. The equivalent circuit model used to fit the electrochemical impedance spectra of the two alloys is shown in Fig. 7. R_s is the solution resistance; R_{ct} refers to the charge transfer resistance; Q_{dl} refers to the double electric layer capacitance at the interface between matrix and solution (capacitance ring in the high-frequency region). R_f and Q_f are film resistor and capacitor (capacitor rings

in the mid-frequency region), respectively. R_L and L stand for resistance and inductance, respectively, being used to describe low-frequency inductive circuits or the onset of localized corrosion. In the current study, proper fitting is carried out on Zsimpwin software, and the estimated results are listed in Table 4. One can see that R_{ct} of $\text{MgZn}_2\text{Y}_{2.66}$ is much higher than $\text{MgZn}_2\text{Gd}_{2.66}$, suggesting that $\text{MgZn}_2\text{Y}_{2.66}$ alloy has relatively higher corrosion resistance. This is consistent with the immersion test and the potentiodynamic polarization test. Furthermore, the R_f value $\text{MgZn}_2\text{Y}_{2.66}$ is much higher than $\text{MgZn}_2\text{Gd}_{2.66}$, suggesting that the corrosion product layer on the $\text{MgZn}_2\text{Y}_{2.66}$ alloy has higher resistance than that on the $\text{MgZn}_2\text{Gd}_{2.66}$ alloy. The result well agrees with the OCP analysis.

3.2.3 Corrosion Products Analysis

XPS was conducted to determine the composition of the collected corrosion products. The XPS survey spectra reveal the existence of Mg, O, and Y elements in $\text{MgZn}_2\text{Y}_{2.66}$ alloy (Fig. 8a), and Mg, O, and Gd elements in $\text{MgZn}_2\text{Gd}_{2.66}$ alloy (Fig. 8b). The Mg 1s peak in the high-resolution spectra can be divided into two sub-peaks: $\text{Mg}(\text{OH})_2$ and MgO . Based on the XPS results, the corrosion products are mainly composed of $\text{MgO}/\text{Mg}(\text{OH})_2$ and Y_2O_3 in the $\text{MgZn}_2\text{Y}_{2.66}$ alloy (Fig. 8c, e), while the corrosion products consist of Gd_2O_3 ,

Table 4 Parameters obtained by fitting the EIS shown in Fig. 6 using the equivalent circuit as shown in Fig. 7

Alloy	R_s ($\Omega \text{ cm}^2$)	R_L ($\Omega \cdot \text{cm}^2$)	L ($\text{H} \cdot \text{cm}^2$)	Q_f ($\Omega^{-1} \text{ cm}^{-2} \text{ S}^n$)	N_f	R_f ($\Omega \cdot \text{cm}^2$)	Q_{dl} ($\Omega^{-1} \text{ cm}^{-2} \text{ S}^n$)	N_{dl}	R_{ct} ($\Omega \cdot \text{cm}^2$)
$\text{MgZn}_2\text{Y}_{2.66}$	9.132	1339	2513	3.66×10^{-3}	0.92	192	1.46×10^{-5}	0.91	562.3
$\text{MgZn}_2\text{Gd}_{2.66}$	8.68	452.2	62.25	2.50×10^{-5}	0.91	57.63	1.10×10^{-7}	0.86	75.32

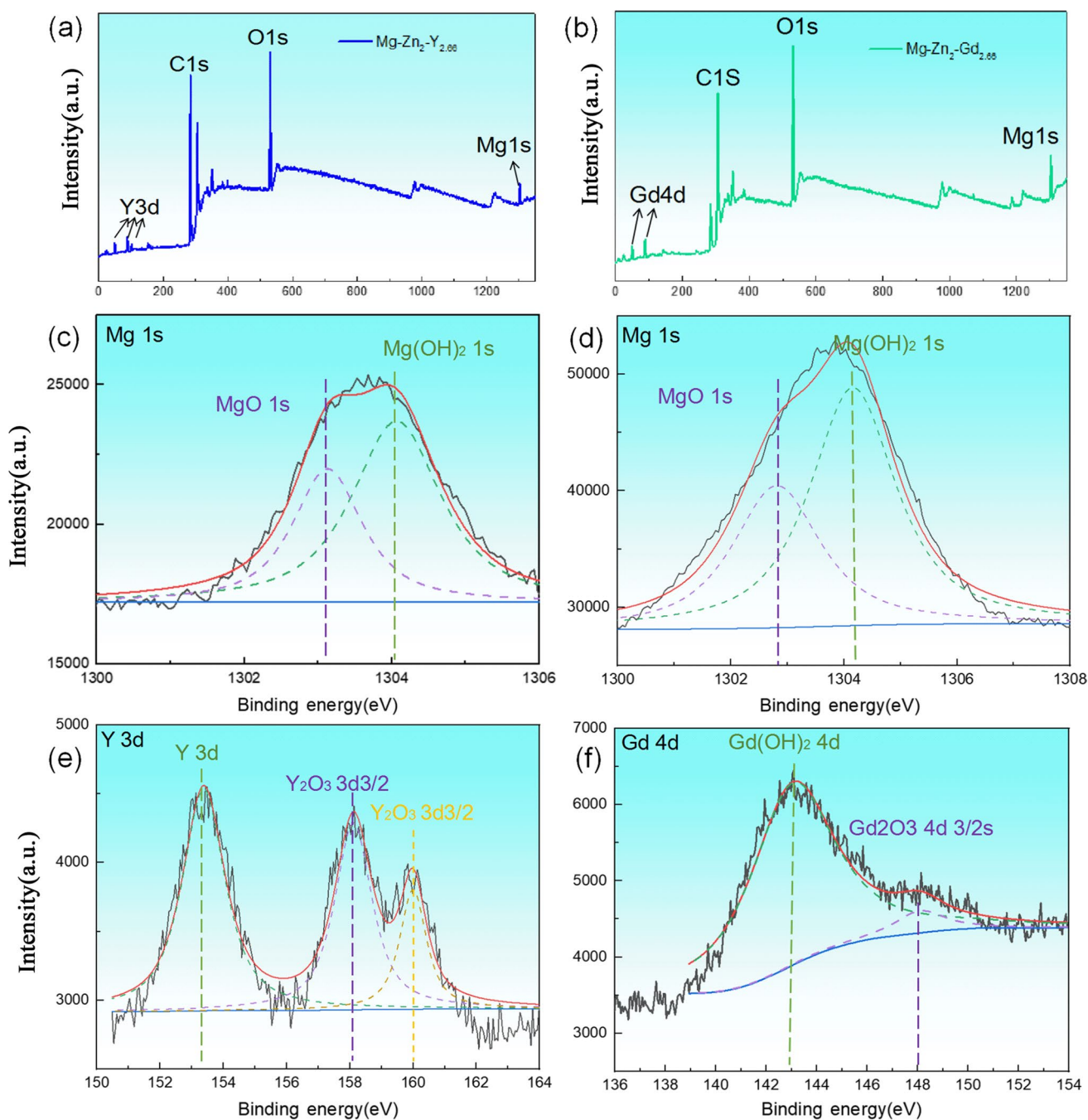


Fig. 8 XPS survey spectra of the corrosion products: **a** $\text{MgZn}_2\text{Y}_{2.66}$, **b** $\text{MgZn}_2\text{Gd}_{2.66}$. High-resolution XPS for **c** Mg 1s and **e** Y 3d of $\text{MgZn}_2\text{Y}_{2.66}$, **d** Mg 1s and **f** Gd 4d of $\text{MgZn}_2\text{Gd}_{2.66}$

$\text{Gd}(\text{OH})_2$, $\text{MgO}/\text{Mg}(\text{OH})_2$ in the $\text{MgZn}_2\text{Gd}_{2.66}$ alloy (Fig. 8d, f).

3.2.4 Corrosion Morphology

The surface morphology of the two alloys after immersion for 300 min ($\text{MgZn}_2\text{Y}_{2.66}$) and 170 min ($\text{MgZn}_2\text{Gd}_{2.66}$), respectively, in the 3.5 wt% NaCl solution were examined

to understand the corrosion mechanism (the corrosion products were removed), as shown in Fig. 9. It can be seen from Fig. 9a, c that there are regularly arranged Y and Zn-rich elements on the alloy surface, and the surface distribution patterns of Y and Zn are similar. According to Fig. 1, many LPSO phase remains on the surface of the Mg–Zn–Y alloy after corrosion, indicating that the corrosion rate of the LPSO is lower than that of the magnesium matrix on the

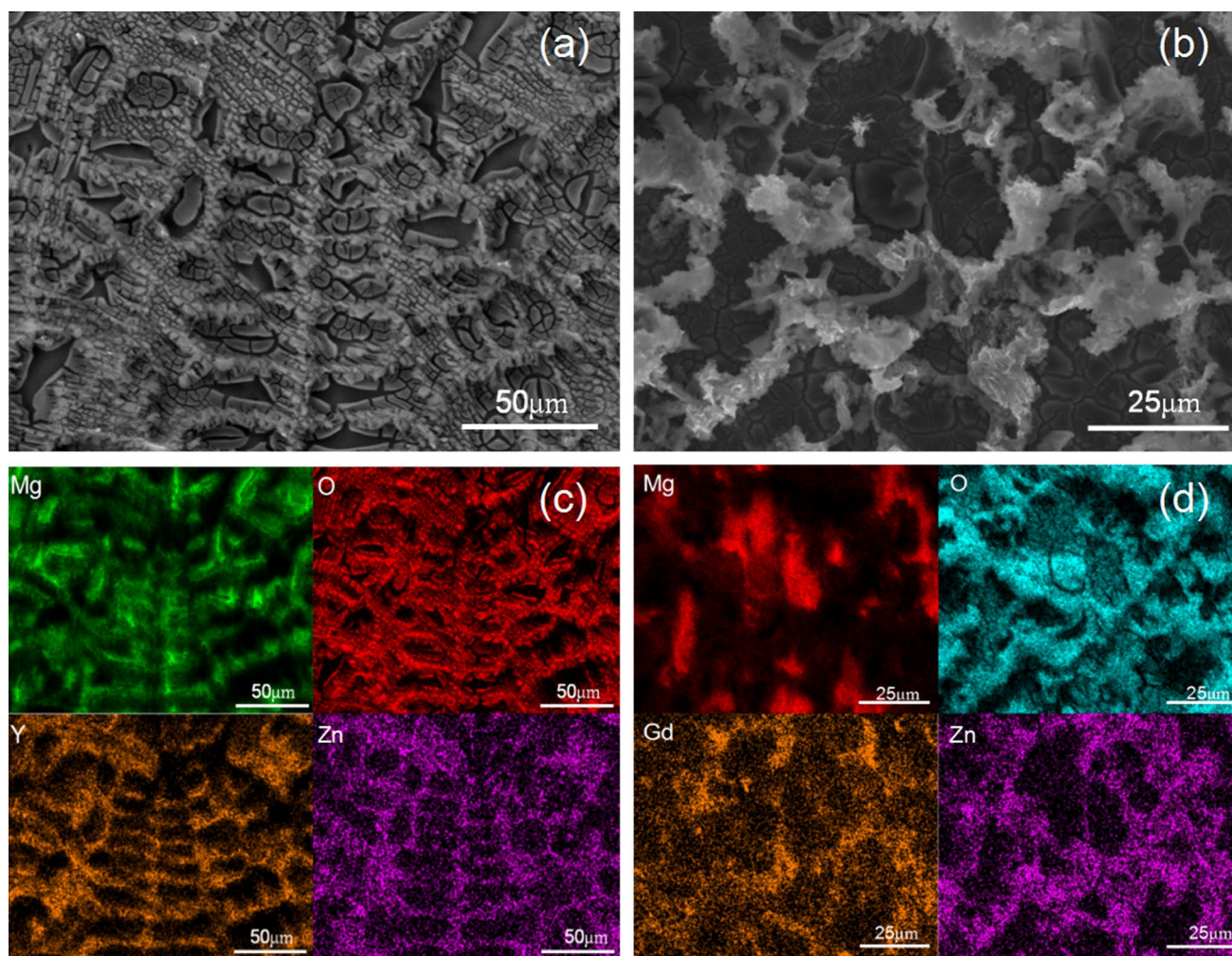


Fig. 9 Microscopic corrosion morphologies of the two alloys after immersion in 3.5 wt% NaCl solution: **a, c** $\text{MgZn}_2\text{Y}_{2.66}$ for 300 min, **b, d** $\text{MgZn}_2\text{Gd}_{2.66}$ for 170 min

one hand, and the corrosion degree of the whole alloy is not severe on the other hand. It can be seen from Fig. 9b, d that there are randomly arranged Gd and Zn-rich substances on the alloy surface, and the surface distribution of the two elements is quite different. According to Fig. 1, the residual substances on the surface of the Mg–Zn–Gd alloy are related to the W phase. These W phase-related Gd and Zn-rich materials are randomly distributed and have different shapes. This suggests that although W has a lower corrosion rate than the Mg matrix, the W phase itself has also undergone certain corrosion damage during the immersion process. In addition, the corrosion attack of alloy is severe. Perhaps, the W phase at different depths was accumulated after corrosion, leading to the distribution pattern of Gd and Zn-rich substances different from that of the original W phase.

In order to further understand the corrosion mechanism of the two alloys, the cross sections of the alloys after immersion in 3.5 wt% NaCl solution for short term and long term

were observed (without removing corrosion products). The cross sections morphology of the alloys after immersion for 5 min was shown in Fig. 10. On the surfaces of $\text{MgZn}_2\text{Y}_{2.66}$ alloy, a corrosion products layer of ~520 nm thickness was formed, which mainly resulted from uniform corrosion of the Mg matrix, as shown in Fig. 10a. In contrast, the corrosion product layer on the surface of $\text{MgZn}_2\text{Gd}_{2.66}$ alloy is about 200 nm thickness, which is much thinner than that on the surface of $\text{MgZn}_2\text{Y}_{2.66}$ alloy. Furthermore, the corrosion products on the surfaces of the LPSO phase (indicated by the orange arrow) are very thin and there is a localized corrosion site within the LPSO phase (indicated by the red arrow). This suggests that although the LPSO phase is cathodic to the Mg matrix, the Mg-rich layers within the LPSO phase are also susceptible to corrosion attack.

Figure 11 shows the cross-sectional morphology of the $\text{MgZn}_2\text{Y}_{2.66}$ alloy after immersion for 5 h. As can be seen from Fig. 11a, although immersion time is as much as 5 h,

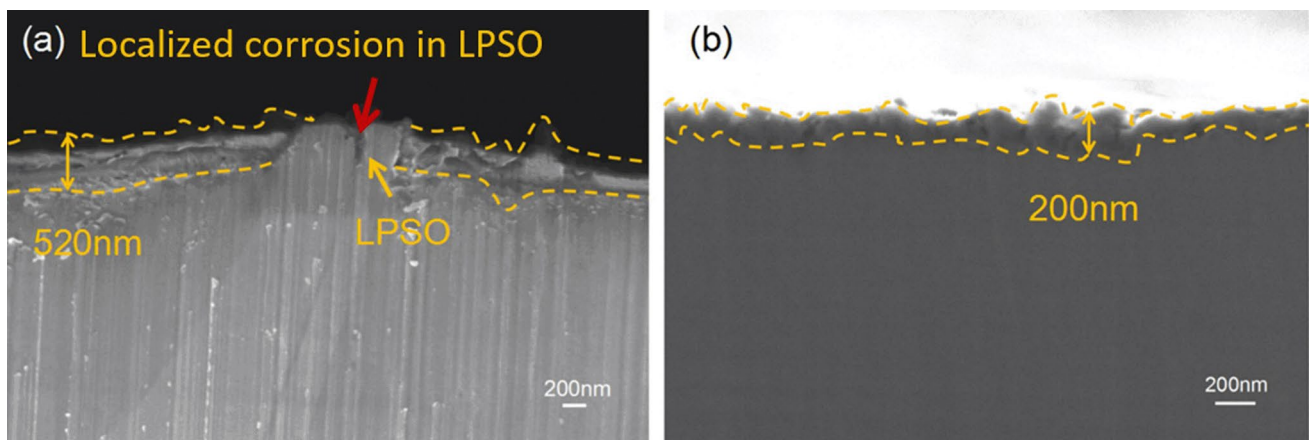


Fig. 10 Cross-sectional morphologies of the alloys after immersion in 3.5 wt% NaCl solution for 5 min: **a** $\text{MgZn}_2\text{Y}_{2.66}$, **b** $\text{MgZn}_2\text{Gd}_{2.66}$

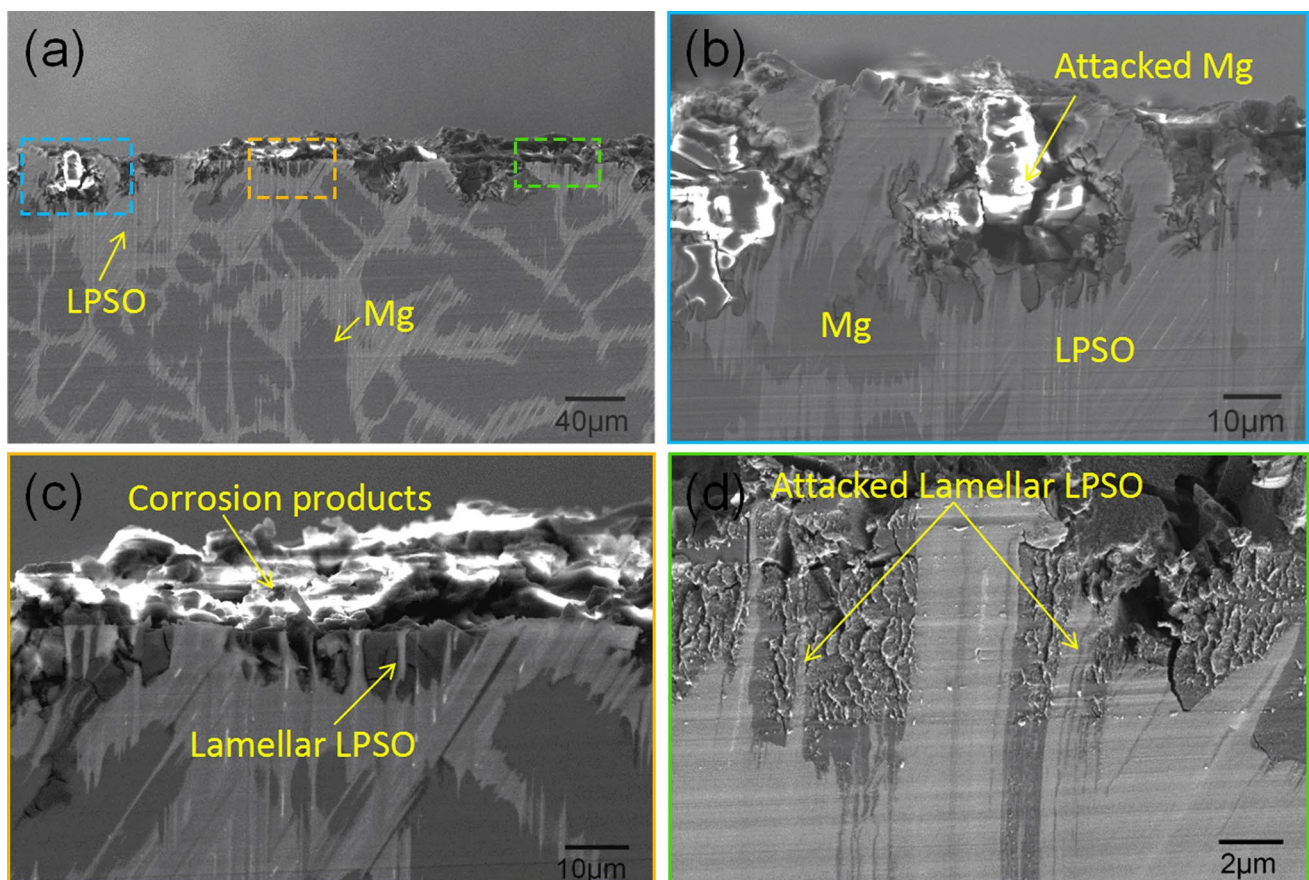


Fig. 11 **a** Low magnification cross-sectional morphology of the $\text{MgZn}_2\text{Y}_{2.66}$ alloys after immersion in 3.5 wt% NaCl solution for 5 h; **b–d** the high-magnification micrographs of blue, orange and green rectangle regions in **a**, respectively

the corrosion attack of the alloy mainly concentrated on the surface, and the corrosion front mostly stopped at the Mg/LPSO phase interface. In Fig. 11b, c, the continuous network of LPSO acts as an obstacle in the corrosion propagation path, which effectively prevents corrosion from propagating

along the Mg matrix into the depth. Interestingly, Fig. 11d shows that corrosion can spread in certain directions within the LPSO phase. It is worth pointing out that the interior of LPSO phase is composed of Zn/Y layers and Mg-rich layers. Therefore, it is inferred that the Mg-rich layers in LPSO

phase would also undergo anodic dissolution, just like the Mg matrix.

In contrast to the $\text{MgZn}_2\text{Y}_{2.66}$ alloy, severe corrosion attack occurred on the surface of the $\text{MgZn}_2\text{Gd}_{2.66}$ alloy only after immersion for 3 h, and there was no obvious relationship between the corrosion front and the distribution of W phase (Fig. 12a). Observations at higher magnifications are shown in Fig. 12b–d. It can be clearly seen from Fig. 12a–d that the W phase is more resistant to corrosion than the Mg matrix, but the W phase will still be destroyed as the corrosion progresses. Further, it is clearly shown in Fig. 12c, d that a tunnel passing through the W phase and connecting two neighboring grains was developed, suggesting that the W phase network failed to stop corrosion propagation.

4 Discussion

It has been demonstrated that the $\text{MgZn}_2\text{Y}_{2.66}$ alloy is much more corrosion resistant than the $\text{MgZn}_2\text{Gd}_{2.66}$ alloy, but the mechanism for this phenomenon is still unknown and

deserves further discussion. In early stages of immersion, both alloys mainly suffered from uniform corrosion. In this case, the corrosion resistance of the alloy can be indirectly reflected by the characteristics of the corrosion product layer formed after uniform corrosion. According to Table 2, the Mg matrix of the two alloys contains similar amount of alloying elements, with the major difference in the type of RE element. The XPS analysis (Fig. 8) indicates that, in addition to $\text{MgO}/\text{Mg}(\text{OH})_2$, the $\text{MgZn}_2\text{Y}_{2.66}$ alloy has Y_2O_3 in its corrosion product layer while the $\text{MgZn}_2\text{Gd}_{2.66}$ alloy has Gd_2O_3 and $\text{Gd}(\text{OH})_2$. Such compositional difference in corrosion product layer should be, to some degree, responsible for the different responses of the two alloys during electrochemical measurement. Further, Fig. 10 shows that the corrosion product layer on $\text{MgZn}_2\text{Y}_{2.66}$ alloy is thicker than that on the $\text{MgZn}_2\text{Gd}_{2.66}$ alloy. This is probably associated with the different phase particles in the two alloys.

It has been reported [37] that the potential difference between the LPSO phase and the Mg matrix is 250 mV in Mg–Y–Zn alloy, while the potential difference between W phase and the Mg matrix is 120 mV in Mg–Zn–Gd–Zr

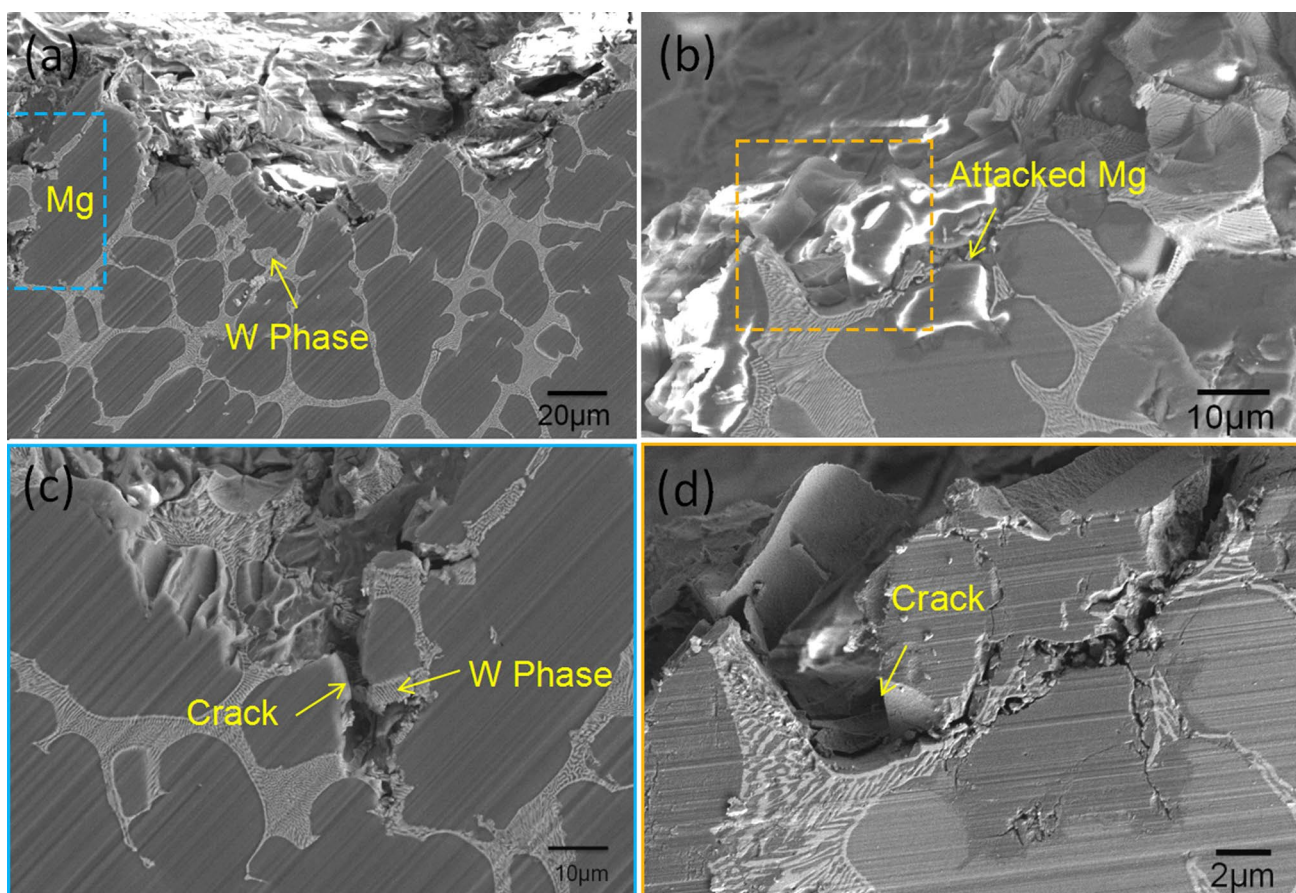


Fig. 12 Low magnification **a** and high magnification **b** cross-sectional morphologies of the $\text{MgZn}_2\text{Gd}_{2.66}$ alloys after immersion in 3.5 wt% NaCl solution for 3 h; **c** the high-magnification micrograph of blue rectangle region in **a**, **d** the high-magnification micrograph of orange rectangle region in **b**

alloy [38]. Therefore, the LPSO phase in $\text{MgZn}_2\text{Y}_{2.66}$ alloy would trigger more severe galvanic corrosion than the W phase in the $\text{MgZn}_2\text{Gd}_{2.66}$ alloy. In the initial stage of immersion, the LPSO phase in the $\text{MgZn}_2\text{Y}_{2.66}$ alloy would hardly be corroded. Uniform corrosion of the Mg matrix led to the formation of a relatively thick corrosion product layer. As for the $\text{MgZn}_2\text{Gd}_{2.66}$ alloy, the uniform corrosion rate is relatively low and corrosion product layer is relatively thin, due to relatively weaker galvanic coupling effect between the W phase and Mg matrix.

With the extension of immersion time, the corrosion gradually changed from uniform corrosion to localized corrosion, as seen in Fig. 3. According to the surface morphology of the removed corrosion products, it can be seen that although LPSO and W phases are both cathodes, they will experience different degrees of corrosion, and LPSO phase is more corrosion resistant than W phase. More importantly, LPSO phase has a strong corrosion barrier effect, which can effectively prevent propagation of localized corrosion from one grain to surrounding grains, as shown in Fig. 11. Since localized corrosion could also occur within the LPSO phase, it is possible that the electrolyte can penetrate the LPSO block through the Mg-rich layers within the LPSO phase, leading to corrosion attack of beneath alloy matrix. However, as reported previously, the volume fraction of the LPSO phase in the $\text{MgZn}_2\text{Y}_{2.66}$ alloy is close to 50%, which can guarantee a very low corrosion propagation rate, even after immersion in the NaCl solution for 24 h [39]. In contrast, the W phase has almost no blocking effect on the propagation of localized corrosion, as suggested in Fig. 12. Besides, once localized corrosion propagates into the alloy matrix, an occluded micro-cell will be formed, further accelerating corrosion attack of the alloy. This explains why the corrosion rate of the $\text{MgZn}_2\text{Gd}_{2.66}$ alloy is much higher than that of the $\text{MgZn}_2\text{Y}_{2.66}$ alloy, particularly between 2 and 8 h of immersion in the NaCl solution. In the late stages of immersion, e.g., 8 h or longer, the $\text{MgZn}_2\text{Gd}_{2.66}$ alloy was so severely corroded that many corrosion products deposited on the alloy surface, which might slow down the mass exchange between the electrolyte and the alloy, resulting in mild reduction of the corrosion rate.

5 Conclusions

In the present study, the effect of yttrium (Y) and gadolinium (Gd) on the corrosion behavior of RE-containing magnesium alloys was systematically studied. Particular attention was focused on the difference in composition of the corrosion products and the role of second phases in the two alloys. The main findings are as follows:

1. The microstructure of as-cast $\text{MgZn}_2\text{Y}_{2.66}$ and $\text{MgZn}_2\text{Gd}_{2.66}$ alloys is mainly composed of Mg matrix and the second phases. The second phase in the $\text{MgZn}_2\text{Y}_{2.66}$ alloy is the Mg_{12}YZn (LPSO) phase, while the second phase in the $\text{MgZn}_2\text{Gd}_{2.66}$ alloy is the $(\text{Mg,Gd})_3\text{Zn}$ (W) phase.
2. The corrosion behavior of the two alloys is similar when immersed in 3.5% NaCl solution. In early stages, uniform corrosion dominated the corrosion process and the corrosion rate is relatively low. After exposed to the NaCl for about 15 min, localized corrosion gradually became dominated and the corrosion rate started to increase. However, corrosion rate of the $\text{MgZn}_2\text{Gd}_{2.66}$ alloy is much higher than that of the $\text{MgZn}_2\text{Y}_{2.66}$ alloy after prolonged exposure, e.g., 60 min.
3. In early stages, the corrosion product layer on the $\text{MgZn}_2\text{Y}_{2.66}$ alloy surface is relatively thick and composed of MgO/Mg(OH)_2 and Y_2O_3 , while the corrosion products on the $\text{MgZn}_2\text{Gd}_{2.66}$ alloy are relatively thin and consists of Gd_2O_3 , Gd(OH)_2 and MgO/Mg(OH)_2 . This is one reason for the high corrosion resistance of the $\text{MgZn}_2\text{Y}_{2.66}$ alloy. After prolonged exposure, the network of LPSO phase in the $\text{MgZn}_2\text{Y}_{2.66}$ alloy can effectively prevent corrosion from propagating within Mg matrix while the W phase in $\text{MgZn}_2\text{Gd}_{2.66}$ does not have such effect, which is another reason for the high corrosion resistance of the $\text{MgZn}_2\text{Y}_{2.66}$ alloy.

Acknowledgements This work was financially supported by the Science and Technology Research Program of Chongqing Municipal Education Commission (KJQN202001106); the Scientific Research Foundation of Chongqing University of Technology (2019ZD32); the China Postdoctoral Science Foundation (2021M700556); the Natural Science Foundation of Chongqing (cstc2021jcyj-bshX0114, cstc2021ycjh-bgzxm0184); the Chongqing Talent Plan: Leading Talents in Innovation and Entrepreneurship (CQYC201903051); the University Innovation Research Group of Chongqing (CXQT20023).

Data availability statement The data presented in our study are available on request from the corresponding author. The data are not publicly available because pertain to a research still in development.

Declarations

Conflict of interest The authors state that there are no conflicts of interest to disclose.

References

- [1] M. Yamasaki, Z.M. Shi, A. Atrens, A. Furukawa, Y. Kawamura, *Corros. Sci.* **200**, 110237 (2022)
- [2] H. Xie, G.H. Wu, X.L. Zhang, Z.Q. Li, W.C. Liu, L. Zhang, X. Tong, B.D. Sun, *Acta Metall. Sin.-Engl. Lett.* **35**, 922 (2022)
- [3] X.C. Ma, S.Y. Jin, R.Z. Wu, J.X. Wang, G.X. Wang, B. Krit, S. Betsofen, *Trans. Nonferrous Met. Soc.* **31**, 3228 (2021)

- [4] P.D. Huo, F. Li, R.Z. Wu, R.H. Gao, A.X. Zhang, *Mater. Des.* **219**, 110696 (2022)
- [5] X.R. Chen, Q.Y. Liao, Q.C. Le, Q. Zou, H.N. Wang, A. Atrens, *Electrochim. Acta* **348**, 136315 (2020)
- [6] X. Gao, J.F. Nie, *Scr. Mater.* **58**, 619 (2008)
- [7] S.Z. Wu, T. Nakat, G.Z. Tang, C. Xu, X.J. Wang, X.W. Li, X.G. Qiao, M.Y. Zheng, L. Geng, S. Kamado, G.H. Fan, *J. Mater. Sci. Technol.* **73**, 66 (2021)
- [8] Z.J. Yu, X. Xu, A. Mansoor, B.T. Du, K. Shi, K. Liu, S.B. Li, W.B. Du, *J. Mater. Sci. Technol.* **88**, 21 (2021)
- [9] L.L. Zhang, Y.T. Zhang, J.S. Zhang, R. Zhao, J.X. Zhang, C.X. Xu, *Acta Metall. Sin.-Engl. Lett.* **33**, 500 (2020)
- [10] M.C. Liang, H. Zhang, L.F. Zhang, P. Xue, D.R. Ni, W.Z. Wang, Z.Y. Ma, H.Q. Ye, Z.Q. Yang, *Acta Metall. Sin.-Engl. Lett.* **34**, 12 (2021)
- [11] S.Y. Xu, C.M. Liu, Y.C. Wan, G. Zeng, Y.H. Gao, S.N. Jiang, *Trans. Nonferrous Met. Soc.* **31**, 1291 (2021)
- [12] L.S. Wang, J.H. Jiang, B. Saleh, Q.Y. Xie, Q. Xu, H. Liu, A.B. Ma, *Acta Metall. Sin.-Engl. Lett.* **33**, 1180 (2020)
- [13] D. Wang, S.J. Liu, R.Z. Wu, S. Zhang, Y. Wang, H.J. Wu, J.H. Zhang, L.G. Hou, *J. Alloy. Compd.* **881**, 160663 (2021)
- [14] J.A. Liu, S.Q. Shi, L.R. Zhang, *Mater Lett.* **231**, 154 (2018)
- [15] J.F. Wang, W.Y. Jiang, Y. Ma, Y. Li, S. Huang, *Mater. Chem. Phys.* **203**, 352 (2017)
- [16] M. Sabbaghian, R. Mahmudi, K.S. Shin, *Metall. Mater. Trans.* **52**, 1269 (2021)
- [17] C. Zheng, S.F. Chen, R.X. Wang, S.H. Zhang, M. Cheng, *Acta Metall. Sin.-Engl. Lett.* **34**, 248 (2021)
- [18] H.X. Liao, J.H. Kim, T.K. Lee, J.F. Song, J. Peng, B. Jiang, F.S. Pan, *J. Magn. Alloy.* **8**, 1120 (2020)
- [19] X.J. Zhou, Y. Yao, J. Zhang, X.Z. Lu, H. Liu, Z.J. Wu, *Mater. Sci. Eng. A* **794**, 139934 (2020)
- [20] S.M. Zhu, R. Lapovok, J.F. Nie, Y. Estrin, S.N. Mathaudhu, *Mater. Sci. Eng. A* **692**, 35 (2017)
- [21] X. Yang, S.S. Wu, S.L. Lv, L.Y. Hao, X.G. Fang, *J. Alloy. Compd.* **726**, 276 (2017)
- [22] M. Gao, K. Yang, L.L. Tan, Z. Ma, *J. Mater. Sci. Technol.* **81**, 88 (2021)
- [23] D.K. Xu, E.H. Han, Y.B. Xu, *Prog. Nat. Sci.: Mater. Int.* **26**, 117 (2016)
- [24] F.Y. Cao, J. Zhang, K.K. Li, G.L. Song, *Trans. Nonferrous Met. Soc.* **31**, 939 (2021)
- [25] G.J. Gao, M.Q. Zeng, E.L. Zhang, R.C. Zeng, L.Y. Cui, D.K. Xu, F.Q. Wang, M.B. Kannan, *J. Mater. Sci. Technol.* **83**, 161 (2021)
- [26] P.P. Wang, H.T. Jiang, Y.J. Wang, Y. Zhang, J.C. Tao, *Acta Metall. Sin.-Engl. Lett.* **35**, 941 (2022)
- [27] W. Wang, S.Y. Chen, K. Qiao, P. Peng, P. Han, B. Wu, C.X. Wang, J. Wang, Y.H. Wang, K.S. Wang, *Acta Metall. Sin.-Engl. Lett.* **35**, 703 (2022)
- [28] S.Y. Jin, X.C. Ma, R.Z. Wu, T.Q. Li, J.X. Wang, B.L. Krit, L.G. Hou, J.H. Zhang, G.X. Wang, *Int. J. Min. Metall. Mater.* **29**, 1453 (2022)
- [29] X.B. Zhang, Z.X. Ba, Z.Z. Wang, Y.J. Wu, Y.J. Xue, *Mater. Lett.* **163**, 250 (2016)
- [30] X.B. Zhang, J.W. Dai, H. Yang, S. Liu, X. He, Z. Wang, *Mater. Technol.* **32**, 399 (2016)
- [31] A. Srinivasan, Y. Huang, L.C. Mendis, C. Blawert, U.K. Kainer, *Mater. Sci. Eng. A* **595**, 224 (2014)
- [32] J. Liu, L.X. Yang, C.Y. Zhang, B. Zhang, T. Zhang, Y. Li, K.M. Wu, F.H. Wang, *J. Alloy. Compd.* **782**, 648 (2019)
- [33] D.K. Bae, S.H. Kim, D.H. Kim, W.T. Kim, *Acta Mater.* **50**, 2343 (2002)
- [34] M.M. Hoseini, R. Mahmudi, R.P. Babu, P. Hedstron, *J. Alloy. Compd.* **831**, 154766 (2020)
- [35] K. Wang, J.F. Wang, X.X. Dou, Y.D. Huang, N. Hort, S. Gavras, S.J. Liu, Y.W. Cai, J.X. Wang, F.S. Pan, *J. Mater. Sci. Technol.* **52**, 72 (2020)
- [36] R. Pinto, M.G.S. Ferreira, M.J. Carmezim, M.F. Montemor, *Electrochim. Acta* **56**, 1535 (2011)
- [37] J.S. Xie, J.H. Zhang, Z.H. You, S.J. Liu, K. Guan, R.Z. Wu, J. Wang, J. Feng, *J. Magn. Alloy* **9**, 41 (2021)
- [38] S.Q. Yin, W.C. Duan, W.H. Liu, L. Wu, J.M. Yu, Z.L. Zhao, M. Liu, P. Wang, J.Z. Cui, Z.Q. Zhang, *Corros. Sci.* **166**, 108419 (2020)
- [39] G.Q. Xi, Y. Mou, Y.L. Ma, X.H. Zhao, J. Xiong, K. Ma, J.F. Wang, *Trans. Nonferrous Met. Soc.* (2022). <https://kns.cnki.net/kcms/detail/43.1239.TG.20220331.1329.020.html>

Springer Nature or its licensor holds exclusive rights to this article under a publishing agreement with the author(s) or other rightsholder(s); author self-archiving of the accepted manuscript version of this article is solely governed by the terms of such publishing agreement and applicable law.